Relative Distribution of DnaA and DNA in *Escherichia coli* Cells as a Factor of Their Phenotypic Variability

Sharanya K. Namboodiri,[a] Alexander Aranovich,[a] Uzi Hadad,[b] Levi Geber,[c] Mario Feingold,[a,b] Itzhak Fishov[d]#

[a]Department of Physics, Ben Gurion University of the Negev, Beer-Sheva, Israel

[b]Ilse Katz Institute for Nanoscale Science & Technology, Ben Gurion University of the Negev, Beer-Sheva, Israel

[c]Department of Biotechnology Engineering, Ben Gurion University of the Negev, Beer-Sheva, Israel

[d]Department of Life Sciences, Ben Gurion University of the Negev, Beer-Sheva, Israel

Running Head: DnaA and DNA variability in *Escherichia coli* cells

#Address correspondence to Itzhak Fishov, fishov@bgu.ac.il.

Abstract word count: 250 words

Text word count: 7126 words (Methods 1581)

Abstract

Phenotypic variability in isogenic bacterial populations helps them to cope with external stress. This variability can stem from gene expression noise and/or unequal partitioning of low-copy-number freely diffusing proteins during cell division. Some high-copy-number components are transiently associated with almost immobile large assemblies (hyperstructures) and thereby may not be distributed equally. We hypothesize that the hyperstructure organization of bacterial cells can contribute to bacterial phenotypic variability. We focus on nucleoid hyperstructure containing many DNA-associated proteins. Our previous findings suggested that replication initiation timing may be the main source of variability for nucleoid segregation events. To uncover the role of the initiator DnaA in phenotypic variability in *E. coli*, we followed its intra- and intercellular distribution using chromosomally encoded fluorescently tagged DnaA and histone-like HU under their native promoters. The mobility of DnaA is low, corresponding to a diffusion-binding mode, but still one order faster than that of HU. The intracellular distribution of DnaA concentration is homogeneous in contrast to the significant asymmetry in the distribution of HU; the latter leading to unequal DNA content of nucleoids in future daughter compartments. The intercellular variability of HU (CV=26%), DnaA, and their ratio (both with CV=18%) is high. The variable DnaA/DNA may cause a variable replication initiation time (initiation noise). Asynchronous initiation at different oriCs may be, in turn, a plausible origin of the asymmetric DNA distribution. Our findings indicate that the DnaA/DNA ratio is the feature determining the variability of initiation time in *E. coli* rather than each of them separately.

Importance

Phenotypic variability is an important phenomenon of bacterial physiology related to adaptation to environmental stresses and antibiotic resistance, not yet completely understood. This work further examines our hypothesis regarding the role of hyperstructure organization of bacterial cells in this phenomenon, focusing on the nucleoid hyperstructure and the DNA-associated replication initiator DnaA. Exploiting fluorescently tagged proteins, we analyze intra- and intercellular distributions, mobility, and concentration variabilities of DnaA and DNA in the population of *Escherichia coli*. The data obtained indicate that the

DnaA/DNA ratio may define the timing of replication initiation event and the ensuing chromosome segregation. As a result, newborn cells with different DnaA/DNA ratios will display variability in the main cell cycle characteristics.

Keywords

Phenotypic variability, Escherichia coli, DnaA, HU, intracellular distribution, cell content variability, protein mobility

Introduction

Bacterial cells display high phenotypic flexibility in response to environmental changes. Species that grow and multiply via symmetrical cell division (e. g. *E. coli*) eventually generate (presumably) identical daughters. Accordingly, in an isogenic population, all subsequent generations would be expected to display identical phenotypes in an unvarying and homogeneous environment. Experimentally, varying phenotypes appear even under these conditions. Phenotypic variability in isogenic bacterial populations helps them cope with external stresses (1-3), including exposure to antibiotics (4). A detailed analysis of individual cells in a population can reveal and quantify this variability. Current understanding attributes gene expression noise and unequal protein partitioning during cell division the key role in the emergence of this variability (5-7). This is essentially correct in the case of low frequency gene expression, or that of low copy number freely diffusing proteins randomly shared between daughter cells. However, it ignores some high-copy number components that are permanently or transiently associated with large, mostly immobile, assemblies, called hyperstructures (8), and thereby are not freely diffusing. Our hypothesis is that the hyperstructure organization of bacterial cells contributes to bacterial phenotypic variability.

In previous work, we studied the nucleoid hyperstructure that contains numerous DNA-associated proteins (9). We found an increasing asynchrony of nucleoid segregation in a cell lineage after 2-3 divisions from a single cell. In contrast, the segregation synchrony remained high in filamentous lineages wherein the lack of septa allowed the free diffusion of proteins along the filament. Nucleoid partitioning is the consequence of two processes: the ongoing DNA replication and the segregation of newly synthesized DNA strands. The segregation process is timed and, most likely, driven by ongoing chromosome replication (10-13). The segregation timing is therefore determined mainly by the initiation time of chromosome replication and the segregation rate in a cell. Since we found the same segregation rates of nucleoids in dividing and filamentous lineages, the nucleoid segregation asynchrony in different cells implies that the replication initiation time is the main source of variability for the segregation process (9). The initiation time is set by the

interplay between the accumulation of the active form of the replication initiator DnaA and the cell growth (14), whereas a large fraction of DnaA is bound to the nucleoid.

DnaA has approximately three hundred high- and low-affinity binding sites on the chromosome, called DnaA-boxes (15). DnaA exists in ATP-bound (initiation-active) and ADP (inactive) forms, interconversion between which is cell cycle-dependent (16). According to the titration model, initiation begins when the cell reaches the 'critical' mass: the threshold concentration of free DnaA-ATP is achieved after DnaA boxes on the chromosome (comprising the specific datA locus) are saturated by *de novo* synthesized protein (14). In addition, the combination of activation and deactivation regulatory systems (through hydrolysis and exchange of nucleotides) may generate stable oscillations of free DnaA-ATP concentration during the cell cycle (17).

This work examines whether the variability in the number of cell-inherited DnaA and its effective local concentration may serve as an essential source of variability in the replication initiation time and the ensuing chromosome segregation. We use chromosomally encoded DnaA and HU fused with eGFP and mCherry respectively to study the intercellular and intracellular variability of their content in the *E. coli* cell population and the mobility of these proteins. HU and DnaA move slower than freely diffusing proteins because they follow a transient-binding type of diffusion. However, the relatively higher diffusion rate of DnaA allows its equal distribution between daughter cells in contrast to the asymmetric segregation of nucleoids. This leads to a highly variable ratio of DnaA to cellular DNA amounts, and, presumably, to a large variation in the replication initiation time.

Results

1. Spatial distribution of DnaA-GFP and HU-mCherry within *E. coli* cells.

1.1. Colocalization of HU and DnaA is notable in living cells but changes when transcription, translation, or replication are impaired

1.1.a. Fluorescence intensity profiles of HU-mCherry and DnaA-GFP in cells

In this work, we used DnaA with eGFP inserted within the domain II as described (23, 36), and expressed from the chromosomal *dnaA* locus under the native promotor (see Methods, 1.1). Together with the chromosomally encoded HU-mCherry, the fluorescence detected from both proteins reflects their real amounts and distributions within the cell. The double-tagged cells displayed normal growth rate and size distribution (Fig. S1) confirming the good functionality of the modified proteins.

The overall distribution of DnaA in *E. coli* cells was examined firstly by comparing images in phase contrast with the GFP (for DnaA) and mCherry (for HU) fluorescence images and the corresponding intensity profiles (Fig. 1). Typically, the spatial distribution of DnaA fluorescence in untreated cells was wider than that of HU (Fig. 1, upper row) roughly matching the nucleoid(s) contour. This also manifests in the corresponding fluorescence intensity profiles (Fig. 1, right column). However, the relatively large cell volume fraction occupied by nucleoids did not allow reliable distinguishing between nucleoid-associated and free cytoplasmic DnaA. We therefore used various drug treatments to modify the relative volume fraction of nucleoids. The nucleoid appears highly compacted after chloramphenicol (CAM) treatment (18), however, surprisingly, the majority of DnaA fluorescence comes from the cytoplasm, sometimes even being excluded from the nucleoid region (Fig. 1, second row). This phenomenon may be due to the dissociation of the protein from DNA upon CAM treatment and calls for measuring the DnaA mobility to verify whether it is freely diffusing (see Section 2). Alternatively, the arrest of the DNA replication using nalidixic acid (NAL) (19) and the continued cell elongation leads to a remarkable increase in the cytoplasmic fraction, despite the nucleoid being somewhat stretched (Fig. 1, third row). In this case, DnaA

fluorescence fills the entire cytoplasm with a small fraction still concentrated in the area of the nucleoid. Additional CAM treatment of these cells led to moderate nucleoid compaction but did not change the distribution pattern of DnaA (Fig. 1, fourth row). Inhibition of RNA synthesis with rifampicin (RIF) resulted in nucleoid expansion to the entire cell volume (20, 21) and a similar spread out of the DnaA (Fig. 1, last row).

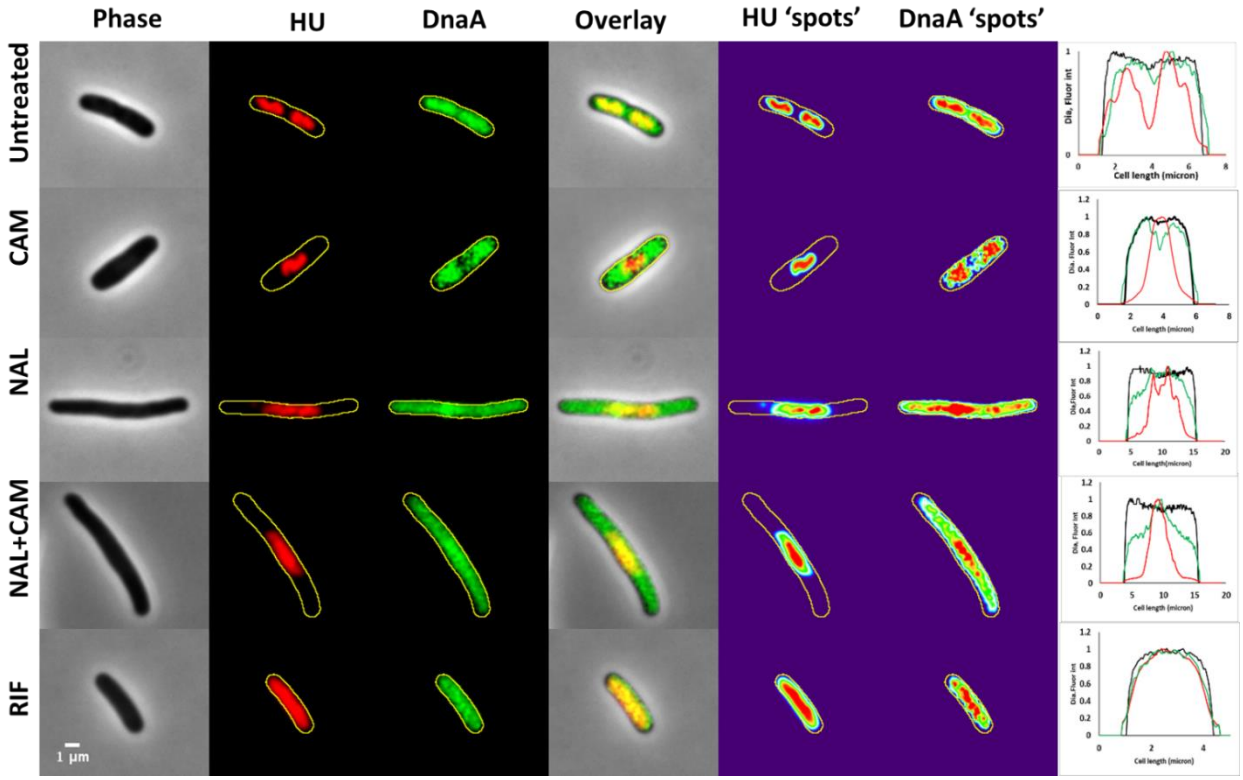

Fig 1. The intracellular distribution of DnaA-GFP and HU-mCherry in a typical cell in different functional states. Phase-contrast images (left column) show the shape and size of the cells. The yellow contour in the HU (red) and DnaA (green) fluorescence images denotes the corresponding cell outline. Overlapping regions of HU and DnaA appear yellow. HU and DnaA 'spots' are revealed using intensity heat maps, where the maximal fluorescence intensity regions appear in red. The profiles along the long axis of a cell (right column) show the normalized diameter of the cell (black line), HU-mCherry intensity (red), and DnaA-GFP intensity (green). Untreated cells (first row) and cells treated with antibiotics (the following rows as designated) are displayed (see Methods for details).

1.1.b. Relative Spots positions

The co-localization analysis is relatively straightforward whenever proteins form clusters visible as distinct fluorescent spots. In our case, the HU-mCherry distribution and, to a larger extent, that of DnaA-GFP are rather wide (see images and profile plots in Fig. 1). While the DnaA distribution is not completely homogeneous, we were not able to identify distinct 'foci' like those previously reported in *E. coli* (22, 23) and *B. subtilis* (24). For HU-mCherry, binding to chromosomes randomly and with low affinity, the highest local intensity merely highlights the maximal DNA density in the nucleoid. In contrast, DnaA has several high-affinity binding sites that may be visible as spots in a fluorescence image (22). HU-mCherry and DnaA-GFP fluorescence maxima (Fig. 1, the 'spots' columns) may be regarded as spots and counted using an appropriate threshold (see Methods). Positions of spots relative to a pole are shown in Fig. 2. In live, untreated cells (Fig. 2, A), HU spots reflect the number of nucleoids in cells of different ages: starting from two nucleoids in short cells and evolving into four nucleoids in the longer ones towards division. The distribution of the number of DnaA spots per cell is similar to that of the number of HU spots (Fig. 2A, inset). DnaA spots display a remarkable position coincidence with HU spots, following the essential overlap of their intensity profiles (Fig. 1, first row). This is confirmed by quantifying distances between related spots (Fig. 2F, dark blue box, and Table 1). The distribution of distances is relatively narrow, with 2/3 of them being within the 0.5 μm range - well within the nucleoid body.

After treatment of cells with CAM, the nucleoids are expectedly compacted and fused pairwise (Fig. 2B, inset), while DnaA is spread across the rest of the cytoplasm (Fig. 1, second row) and most cells lack the DnaA spots (Fig. 2B, inset). The rare DnaA-GFP spots are located 'outside' the zone of the HU-mCherry spots (Fig. 2B), hinting that DnaA-GFP detaches from the compacted nucleoid after CAM treatment. Accordingly, the distribution of distances becomes rather wide (Fig. 2F, orange box) with only a quarter of spot pairs within a 0.5 μm distance (Table 1). In NAL-treated cells with a single nucleoid and a single DnaA spot, there is an overlap of spot positions as seen in live cells (Fig. 2C), despite the remarkable spread of DnaA throughout the cytoplasm (Fig. 1, third row). The distances between corresponding spots are large (Fig. 2F, grey box), but still within the elongated nucleoid. However, when the cells are treated with NAL and afterward with CAM, the DnaA-GFP spots are observed far from the HU-mCherry spots and outside the compacted

nucleoids (Fig. 2D, and F, yellow box). In RIF-treated cells, both DnaA and HU appear to spread throughout the entire cell (Fig. 1, bottom row) and, nevertheless, a single maximum of each protein can be detected as 'spots' using the same threshold as in Figs. 2A-D (Fig. 2E). The distribution of distances between paired HU and DnaA spots is narrower than in the case of both CAM and NAL-treated cells (Fig. 2F, blue box), with about half of the distances being less than 0.5 µm (Table 1).

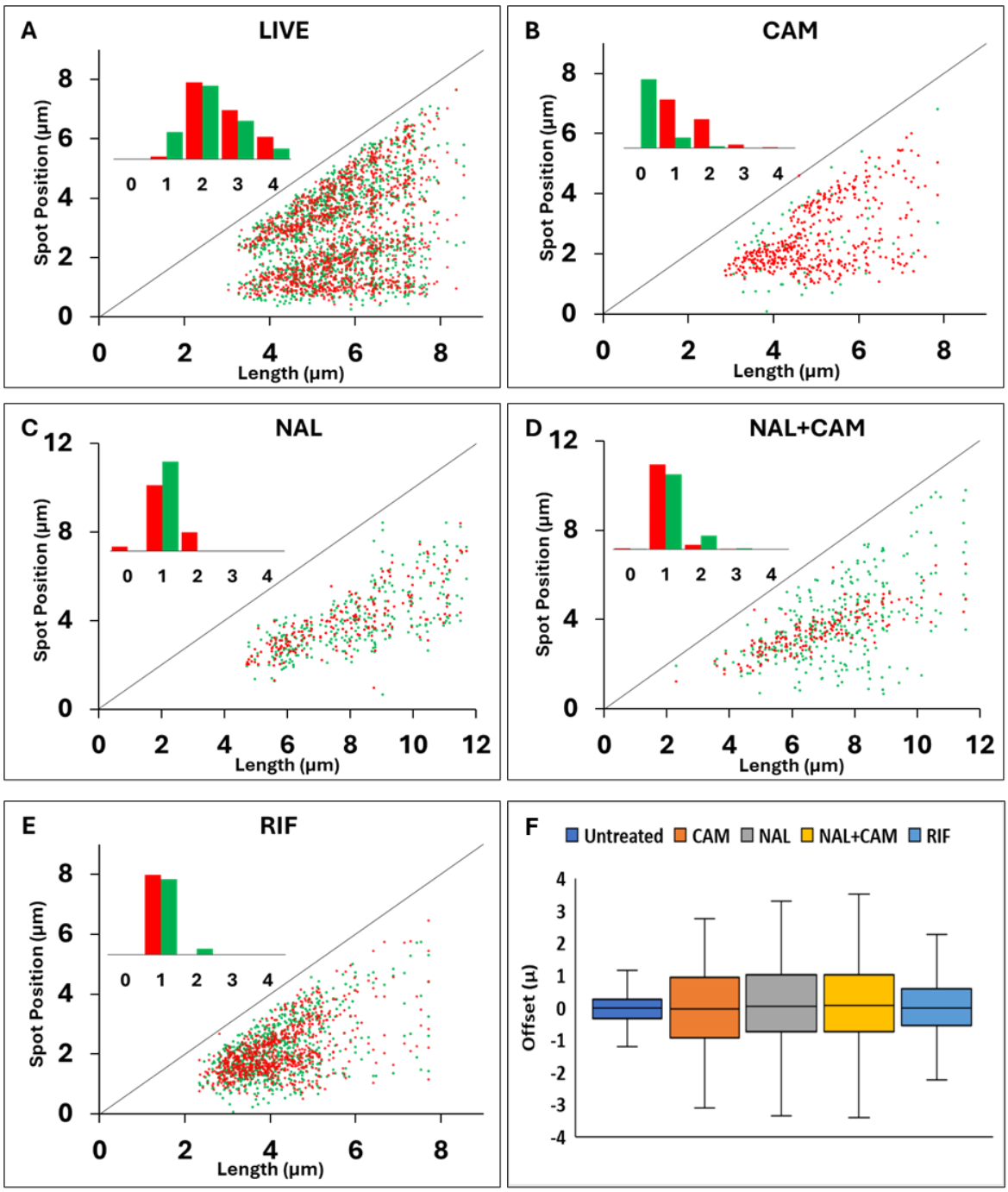

Fig 2. Scatter plots of the fluorescence maxima ('spots') positions of DnaA-GFP (green) and HU-mCherry (red) as a function of cell length. Positions are shown as distances from a pole for a population of approximately 500 cells of various lengths; the diagonal line designates the distance to the opposite pole. Untreated **(A),** CAM-treated **(B),** NAL- and NAL+CAM-treated **(C** and **D),** and RIF-treated populations **(E)** are portrayed. What may appear as double-nucleoid RIF-treated cells in the scatter plot are due to off-centered single maxima in different cells. The distributions of HU and DnaA spot numbers are shown in the insets in each panel. Distributions of distances between paired spots of HU and DnaA in untreated and antibiotic-treated cells are displayed using box plots **(F)**.

Table 1. Percentage of paired HU and DnaA spots positioned within a 0.5 µm vicinity in cells at different functional states.

Cell Treatment	% of paired spots within 0.5 µm vicinity
Untreated	69
CAM	26
NAL	31
CAM+NAL	35
Rif	45

1.1.c. Pixel-wise colocalization

Yet another, more detailed approach to two fluorophores colocalization is the single-cell pixel-to-pixel analysis of their fluorescence intensities (25, 26). The pixel intensity values of the DnaA-GFP and HU-mCherry images from the same cell are displayed as a scatterplot nicknamed cytofluorogram, which uses the respective intensities as coordinates (see Methods, section 2.2). The distribution of the points reflects the extent to which the fluorophores are colocalized. While a positive linear correlation specifies a high degree of colocalization, a high density of points lying close (parallel) to one of the axes corresponds to the absence of colocalization. We also use the Pearson and Mander coefficients as quantitative measures of colocalization (26). The Pearson

coefficient provides the strength and mode of the correlation, while the Manders coefficient gives the degree of overlap between the two species.

The typical cytofluorograms of single cells in different functional states are presented in Fig. 3. First, note the near-perfect colocalization of HU with DAPI (Fig. 3F), confirming that HU-mCherry fluorescence provides an accurate representation of the DNA density: the highest intensities correspond to the nucleoid core, intermediate – the visible nucleoid body, and low – the nucleoid periphery. The cytofluorograms in Figs. 3A-E display the colocalization of DnaA and HU. In a live cell (Fig 3A), many pixels with very low, close-to-background, fluorescence intensities (lower-left corner) correspond to fluorophore/protein-free cell areas. At higher intensities, a linear positive correlation is observed with a Pearson coefficient of about 0.8 (Table S1) suggesting that more DnaA molecules reside at higher nucleoid densities, matching the close vicinity of the corresponding spots (Section 1.1.b, Table 1). The cytofluorogram is rather different in CAM-treated cells (Fig. 3B): most of the pixels within a wide range of DnaA-GFP fluorescence intensities have a very low HU-mCherry fluorescence (laying parallel to the y-axis), indicating that they are located outside the nucleoid. A small fraction of high DnaA-GFP intensities coincides with a wide range of mCherry intensities - within the nucleoid core. The Pearson coefficient value of 0.6 confirms a relatively poor correlation (Table S1). NAL-treated cells have a slightly higher Pearson coefficient than CAM-treated cells (Table S1), again with most of the GFP fluorescence localized elsewhere than the mCherry fluorescence-containing pixels (Fig. 3C). Just part of the fluorophores colocalize according to the positively correlated intensities. Moreover, when the NAL-treated cells are additionally treated with CAM, the Pearson coefficient drops (Table S1), and the distribution of the data points in the cytofluorogram (Fig. 3D) is specific for the absence of colocalization. In RIF-treated cells, the homogeneous spread of both the nucleoid and DnaA-GFP over the cell volume (e. g. Fig. 1, bottom row) results in an almost perfect colocalization with a high Pearson coefficient value (Fig. 3E and Table S1). This, however, is not necessarily an indication of mutually dependent colocalization, since the same cytofluorogram will be obtained for two independent fluorophores homogeneously filling the same volume.

The Manders coefficient is remarkably high for the fraction of HU overlapping DnaA for all functional states. In contrast, the fraction of DnaA, which overlaps HU, is moderately high in live

(untreated) and RIF-treated cells and decreases in cells treated with CAM (consistent with the images of Fig. 1 and the patterns of the cytofluorograms). That means part of DnaA is always associated with the nucleoid, but a large fraction of DnaA resides in the nucleoid periphery in CAM-treated cells. Note that, in NAL-treated cells, the Manders coefficient is cell length-dependent, reflecting the lower nucleoid/cytoplasm ratio in longer cells.

These results suggest colocalization of DnaA with the nucleoid in untreated cells and partially in NAL-treated, in contrast to a significant separation of the protein from the nucleoid occurring in CAM-treated cells.

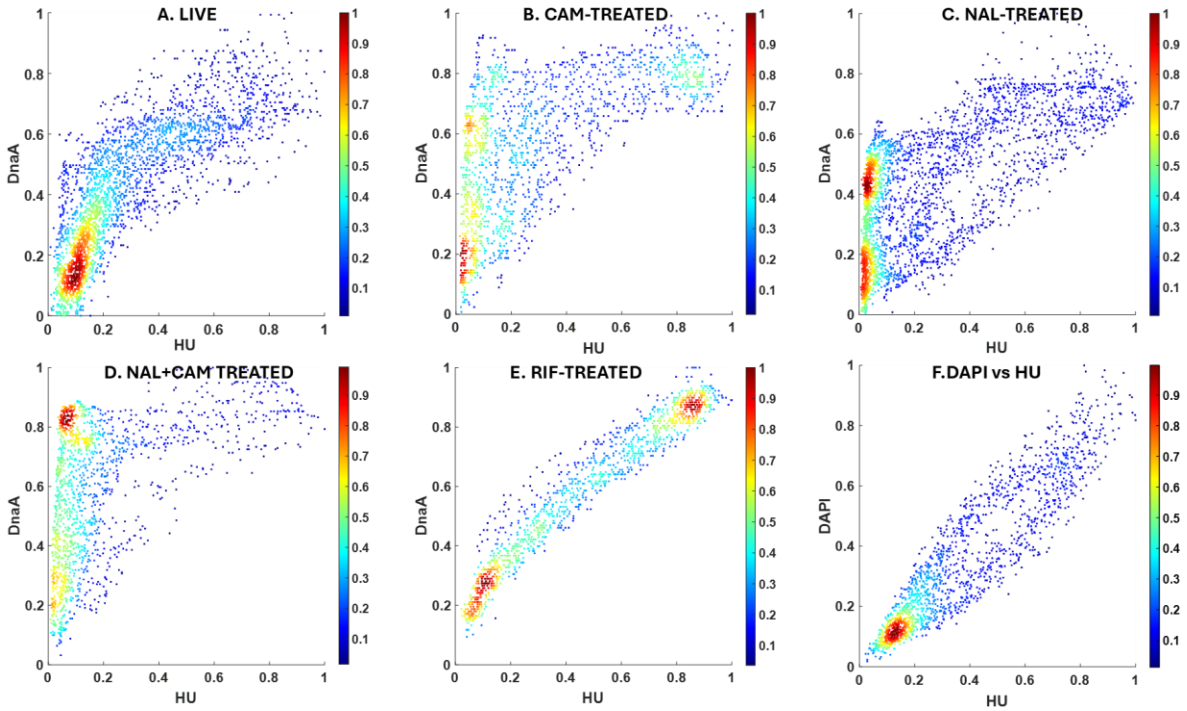

Fig 3. Pixel-intensity-based analysis of DnaA-GFP and HU-mCherry colocalization in cells in different functional states. Cytofluorograms for eGFP and mCherry fluorescence intensities of single cells; live and treated with CAM, NAL, NAL+CAM, or RIF (panels A-E, respectively). In addition, Panel F shows the correlation between HU-mCherry and DAPI fluorescence intensities. All intensities are normalized to the maximal pixel value in each cell. The color coding reflects the relative densities of experimental points in each panel. Cytofluorograms were generated by the JaCoP plugin for ImageJ and plotted using the MATLAB subroutine (see Methods).

1.2. Distribution of HU and DnaA between cell halves - Asymmetry Index

To reveal any asymmetry in the distribution of different components in the two cell halves and correlations between them, both randomly oriented and ordered according to the 'leading' pole cell populations were analyzed (see Methods, Section 3). We define ratios of the amounts/concentrations of these components in the two cell halves as asymmetry indexes. In a random population, the asymmetry indexes for HU, DnaA, and DNA amounts weakly correlate with the volume asymmetry with a wide variation between different cells (Fig. 4A). As expected, the ratios of concentrations of HU-mCherry are well correlated with those of DAPI-stained DNA (Fig. 4B), showing that HU provides a good representation of the DNA distribution in the cell (27). In contrast, the concentration asymmetry of DnaA is only weakly correlated with that of HU, while indexes for volume and HU concentration anti-correlate (Fig. 4B). In a randomly oriented cell population, the average asymmetry index of any variable is understandably close to 1 (Fig. 5, Table 2, Fig. 12 D&F), but the cell-to-cell variability in the population is remarkable (Fig. 4), with CV up to 25% for HU and DAPI (Table 2).

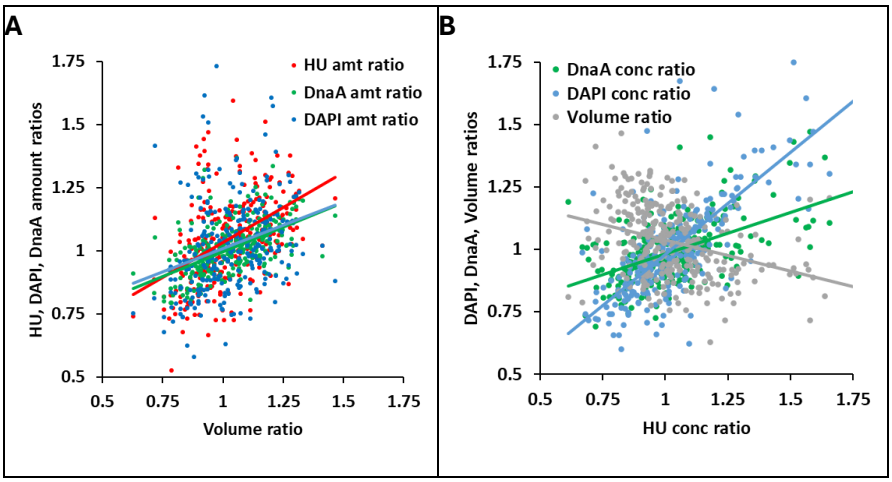

Fig 4. Asymmetry indexes of various components as a function of volume asymmetry (A) and asymmetry of HU concentration (B) in the randomly oriented cell population of 500 live cells. All data were fitted to linear equations as follows. In **A**: y = 0.55x + 0.478 (R=0.4) for HU (red); y = 0.36x + 0.64 (R=0.26) for DAPI (blue); y = 0.36x + 0.64 (R=0.54) for DnaA (green). In **B**: y

= 0.81x + 0.16 (R=0.72) for DAPI (blue); y = 0.33x + 0.64 (R=0.53) for DnaA (green); y = -0.25x + 1.28 (R=0.33) for Volume (dark grey).

Another way to assess the correlation in asymmetry between cell components is to evaluate it in a population aligned according to the cell half containing a larger amount of one of the components ('leading pole', see Methods). Alignments corresponding to either larger diameter or larger HU, DnaA, and DAPI amounts result in respective asymmetry indexes significantly higher than 1 (Fig. 5A, Fig. 12 E&G). The HU, DnaA, and DAPI indexes do not follow the volume alignment in contrast to the implication that the amounts of components with a homogeneous distribution will follow the volume asymmetry. When each of them is chosen as the leading pole for alignment, others do not necessarily follow it. Accordingly, the concentration asymmetry indexes (Fig. 5B) appear inversely asymmetric to the diameter-aligned cells. Notably, cells aligned according to amounts of HU or DAPI display high asymmetry indexes following each other (Fig. 5A) consistent with the correlation found for the random population (Fig. 4A). This asymmetry in the distribution of DNA material between two cell halves also holds for the DNA concentration, in contrast to that of DnaA. Moreover, the DnaA concentration asymmetry index is close to 1 for all types of alignments, meaning its concentration is homogeneous within cells. All concentration asymmetry indexes are summarized in Table 2. The difference between population-wide asymmetries of DnaA and DNA (DAPI or HU) concentrations is highly significant ($p<0.001$) when cells are aligned according to HU or DAPI content. Other asymmetry indexes do not differ significantly. We have also not found a remarkable dependence of asymmetry indexes on the cell size (age) (data not shown). Furthermore, the asymmetry in the distribution of DNA material between cell halves holds also for the wtDnaA MG1655 (*hu-egfp*) strain (Table S2), confirming that it is not caused by a compromised functionality of DnaA-eGFP.

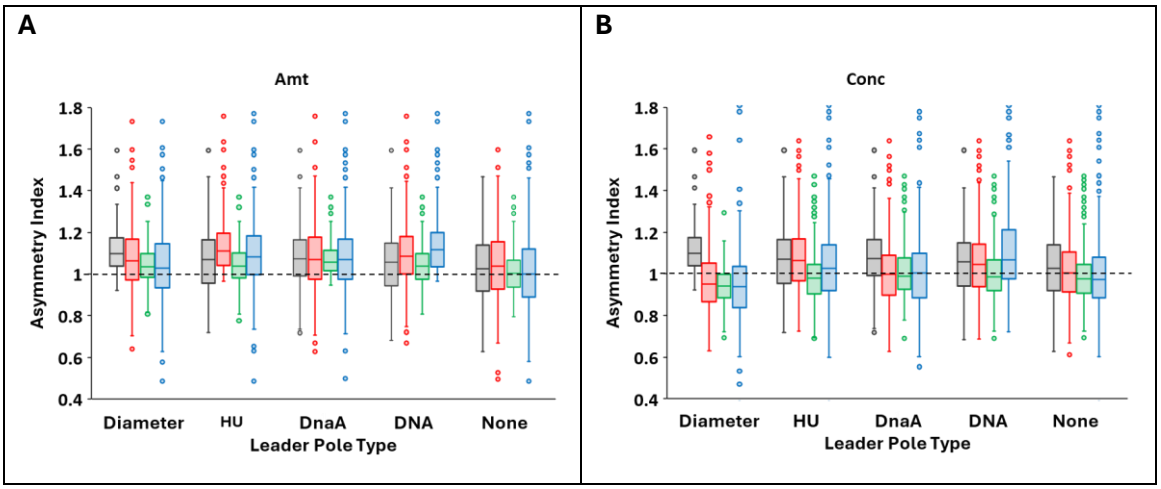

Fig 5. Asymmetry indexes (ratios between two cell halves, see Methods) for cell volume (gray), HU (red), DnaA (green), and DNA (DAPI, blue). The population-wide distributions are shown for different cell alignments using the diameter, HU, DnaA, or DAPI content as leader poles, or unaligned (None). The indexes are calculated for amounts (**A**) and corresponding concentrations (**B**). The same volume asymmetry index is shown in **B** as in **A** for comparison. Note that the population median is shown in these box plots; the average values are presented in Table 2.

Table 2. Population averages (± SD) of concentration asymmetry indexes for different cell alignments (corresponding to Fig. 5B).

Leader pole	Asymmetry index			
	Volume	HU	DnaA	DAPI
Diameter	1.12 ± 0.10	0.95 ± 0.21	0.93 ± 0.10	0.93 ± 0.20
HU	1.03 ± 0.15	1.17 ± 0.25 *	1.02 ± 0.15*	1.13 ± 0.27 *
DnaA	1.06 ± 0.13	1.05 ± 0.28	1.03 ± 0.16	1.04 ± 0.28
DAPI	1.02 ± 0.14	1.14 ± 0.26 *	1.02 ± 0.11*	1.17 ± 0.19 *
None	1.05 ± 0.14	1.03 ± 0.26	0.98 ± 0.14	0.99 ± 0.25

* – $p < 0.001$ for the similarity between DAPI or HU and DnaA asymmetry indexes.

2. Mobility of HU and DnaA is impeded within the cell

To understand the difference in asymmetry in the intracellular distribution of HU and DnaA, the protein mobility was measured by FRAP (see Methods, section 5). The diffusion coefficients of DnaA and HU were measured for live cells and treated with antibiotics. In addition, plasmid-borne eGFP and DNA binding impaired mutant DnaA(L417P)-eGFP expressed in the parent MG1655 strain were used as free diffusing controls.

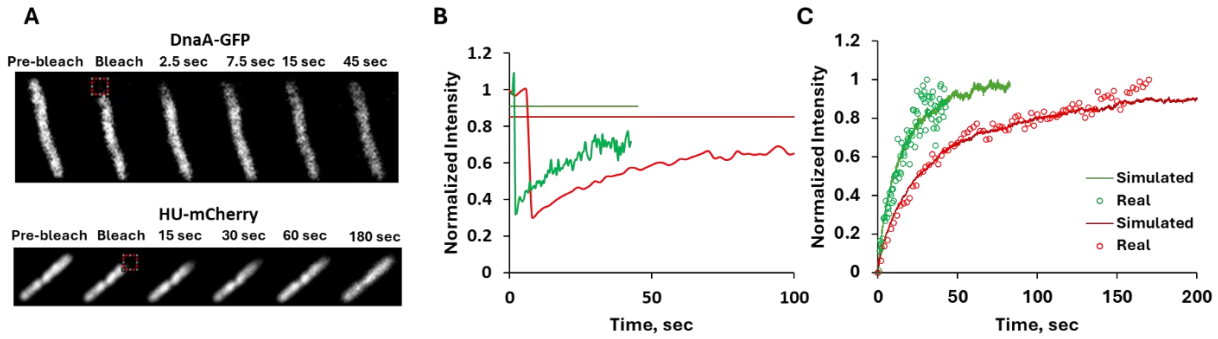

Fig. 6. Example of FRAP experiment with live cells. The cells were bleached on poles (1x1 μm red squares in **A**) and the fluorescence recovery in these areas (**B**, green – DnaA, red - HU) was further analyzed by simFRAP ((28) and see Methods, Section 4) resulting in the diffusion coefficients of 0.102 ± 0.013 μm^2/sec and 0.040 ± 0.001 μm^2/sec for DnaA and HU respectively (**C**, green circles and line – real and simulated DnaA recovery kinetics, red – the corresponding curves for HU). The horizontal lines in **B** show the expected recovery kinetics maxima for DnaA (green) and HU (red).

In live cells (Fig. 6), the mobility of DnaA appeared to be ten times faster than that of HU (Table 3) presumably reflecting their different affinities and number of binding sites on the chromosome. This diffusion coefficient for DnaA is in good agreement with the data of (24) obtained by FRAP and SMT. The diffusion of HU was found much faster by SMT – 0.14-0.38 μm^2/sec for the transition between binding sites (29, 30). The high number of binding sites and the residence time of proteins bound to DNA allow estimation of the diffusion coefficient of 0.04 μm^2/sec for the entire duration of a trajectory (29). This estimation is more relevant for comparison

with the results of the FRAP method. Our rationale behind FRAP was distinguishing the free (cytoplasmic) and the nucleoid-associated DnaA. It was not achievable in live cells because of the large volume fraction occupied by the nucleoid, and the resulting high spatial overlap between the fluorescence of the two proteins (see Section 1.1.a above).

TABLE 3. Summary of protein diffusion rates measured by FRAP.

Protein	Functional state of cells	No. of cells measured	Diffusion coefficient*, $\mu m^2/sec$
DnaA-GFP	Untreated	12	0.310 ± 0.077
	CAM-treated	10	0.089 ± 0.012
	Rif-treated	8	0.080 ± 0.019
	NAL-treated	8	0.060 ± 0.036
HU-mCherry	Untreated	10	0.036 ± 0.006
	CAM-treated	10	0.014 ± 0.005
	Rif-treated	8	0.034 ± 0.002
DnaA(L417P)-GFP	Untreated	7	3.03 ± 0.14
Free GFP	Untreated	2	7.70 ± 0.47

* Averages and standard deviations for the set of cells are shown.

Surprisingly, the diffusion of DnaA in the cytoplasm, outside the nucleoid either highly compacted by the CAM treatment or in elongated cells with replication-arrested nucleoid after NAL treatment, was even slower than in live cells (Fig. 1, Table 3, Supplementary Fig. S2). The same slow diffusion of DnaA was obtained when the nucleoid was spread over the whole cell volume after RIF treatment (Table 3, Supplementary Fig. S2). The low fluorescence intensity of DnaA-GFP, which limits the image acquisition rate, may hamper the detection of fast fractions. As expected, GFP alone and mutant DnaA showed a one-order faster diffusion rate than DnaA, typical for free-diffusing proteins without specific interaction with other structures (31).

3. The binding affinity of DnaA to the nucleoid is weaker than that of HU.

The appearance of DnaA-GFP fluorescence in the cytoplasm, out of the nucleoid, after CAM or NAL treatment (see the Colocalization section) raised the question of the binding affinity of the protein to the nucleoid, assuming the 'cytoplasmic' DnaA is free. We thus compared the DnaA and HU content in the nucleoid body in intact cells and nucleoids released from spheroplasts by measuring the nucleoid-associated fluorescence of DnaA-GFP, HU-mCherry, and DAPI (see Methods, Section 1.2). Typical corresponding images (Fig. 7) display nucleoids enclosed in the envelope or released from exploded spheroplasts. DnaA fluorescence overlaps well with that of HU and DAPI in cells and spheroplasts but is essentially absent in the released nucleoids (Fig. 7, lower right image). Some spheroplast ghosts occasionally collapse back and are still visible in phase contrast (blue arrows), trapping remarkable amounts of proteins, including DnaA (orange arrow) but not HU and DNA. Fig. 8 shows the fluorescence from nucleoids released from spheroplasts in more detail. Namely, HU (B and C) and DAPI (C and D) highlight the nucleoids differently: HU shows up as a cloud with a thread-like texture, while DAPI staining reveals some additional compact structures that are not present in HU-mCherry images. DnaA-GFP is hardly detected in the isolated nucleoid and is visible only within collapsed spheroplasts **(A)**.

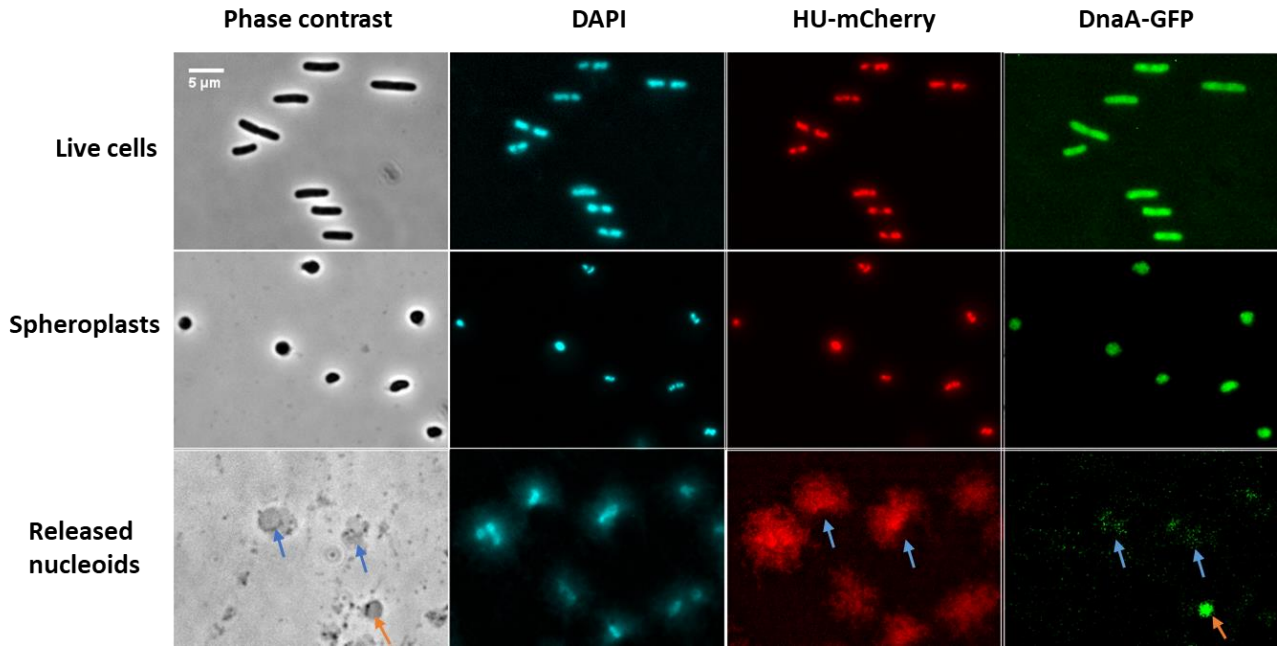

Fig 7. Typical images of cells (upper row), spheroplasts (middle row), and released nucleoids (bottom row) in phase contrast and fluorescence of DAPI-stained DNA (cyan), HU-mCherry (red), and DnaA-GFP (green, from left to right). All fluorescence images were processed with the "enhance contrast" routine. The space bar (5 μm) is the same for all images in the panel.

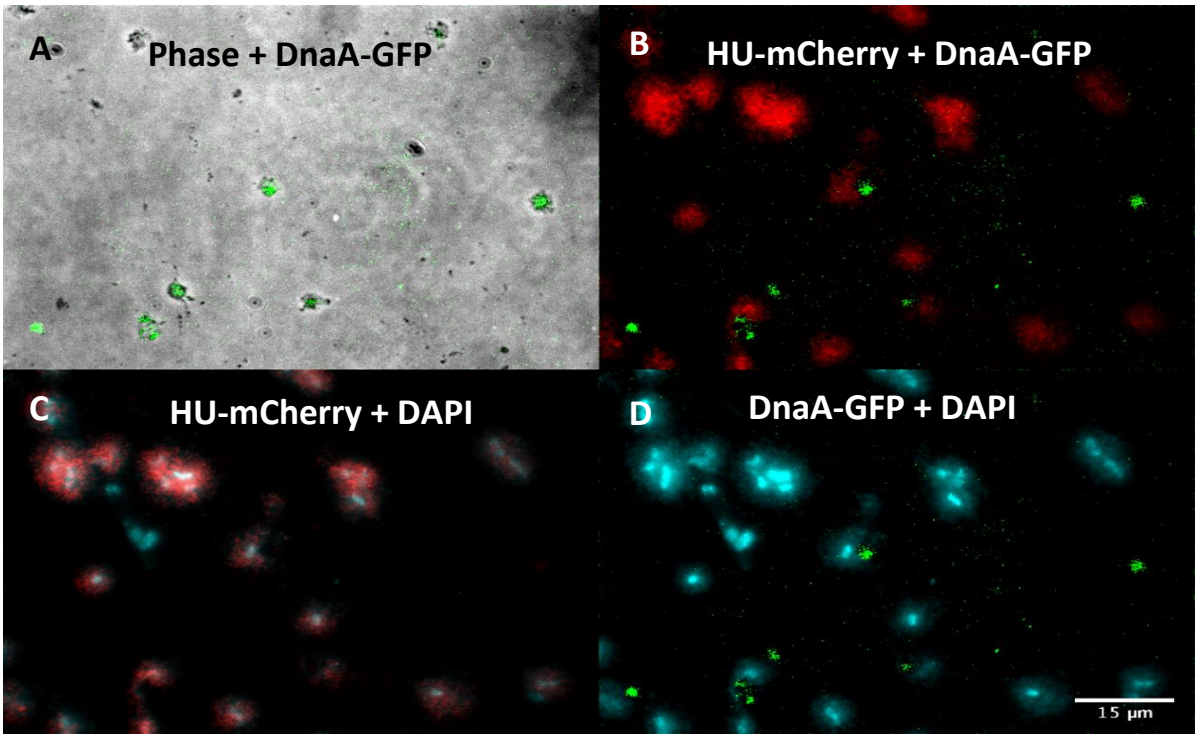

Fig 8. Overlays of phase contrast (gray) and DnaA-GFP (green) (A), HU-mCherry (red) and DnaA-GFP (B), DAPI-stained DNA (cyan) and HU-mCherry (C), and DnaA-GFP and DAPI (D) images of released nucleoids. DnaA-GFP is visible mainly within collapsed spheroplasts **(A)** and is hardly detected in the isolated nucleoids (**B, D**). All fluorescence images were processed with the "enhance contrast" routine before overlaying. The space bar (15 μm) is the same for all images in the panel.

The loss of HU and DnaA from the nucleoid upon its release from spheroplasts is quantitatively presented as changes in the total HU-mCherry and DnaA-GFP fluorescence intensities of a nucleoid relative to that of DAPI. This is in the assumption that the DAPI/DNA ratio is the same in different preparations due to its very high binding affinity (32). Relative to the average amount of DnaA-GFP per nucleoid in intact cells, a loss of 30% of DnaA fluorescence is observed

when the cells are converted to spheroplasts, while that of HU shows only a 6% drop (Fig 9). When the spheroplasts blow up, the DnaA fluorescence of the released nucleoids is reduced by 90%, and about 70% of HU is lost. Thus, the loss in the amount of HU in the isolated nucleoid was less severe, indicative of a stronger association of HU than of DnaA to the nucleoid. This qualitative estimation looks contradictive to the measured values of binding affinity for DnaA and HU to DNA: dissociation constants in a nanomolar range for DnaA (33) and a millimolar range for HU (30). However, while there are about 300 such strong binding sites for DnaA on the chromosome of *E. coli* (15), HU can bind nonspecifically to 10^5 - 10^6 sites over the whole length of the chromosome so that the apparent dissociation constant of HU was estimated in a micromolar range (34). This 'sink' effect results in a long retention time of HU on the nucleoid as a whole (34) and is consistent with the differences in the intracellular diffusion coefficients measured by FRAP (see Results, Section 2).

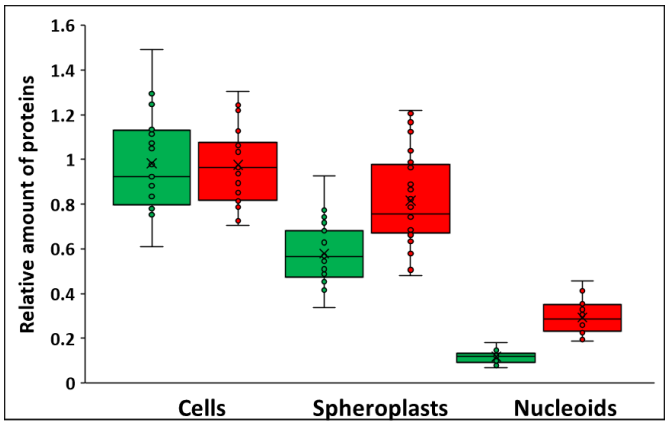

Fig. 9. An estimate of the binding affinity of HU and DnaA to the nucleoid. Box plots of the DnaA-GFP and HU-mCherry integral fluorescence intensities of individual nucleoids relative to the corresponding DAPI fluorescence intensity in cells, spheroplasts, and released nucleoids. The GFP/DAPI and mCherry/DAPI ratios of fluorescence intensities for all samples were normalized to the average intensity ratios of intact cells. Cells MG1655 (*dnaA-gfp, hu-mcherry*) were grown to steady-state, harvested, and permeabilized with 10% methanol for DAPI staining (see Methods for details). Spheroplasts were prepared as described in Methods and stained with DAPI without permeabilization. The nucleoids were released from the spheroplasts heated at 37°C for 10 minutes and loaded on the agarose pads.

4. Intercellular variability in HU and DnaA content in a population

The finding of an asymmetrical distribution of the genetic material between cell halves (Section 1.2 of Results) raised a question about the variability of the DNA and DnaA cell contents in the population. We thus performed an analysis of the cell-to-cell variation in a steady-state culture. The linear correlation between total DnaA-GFP fluorescence and the cell size (Fig. 10, A) and between DnaA and HU (Fig. 10, C) indicates continuous synthesis of DnaA during the cell cycle proportionally to the DNA content. As a result, the concentration of DnaA is cell volume-independent (Fig. 10, D), i.e. it is constant during the cell cycle. This seems in contradiction with the single-time event of initiation of DNA replication, which means that, in general, initiation is not dependent on the overall cellular concentration of DnaA, but rather on the concentration of its activated free form. Yet, the DnaA concentration varies from cell to cell of the same volume (CV~18%) (Fig. 10, D, Table 4). The HU cellular content is also proportional to the cell volume (Fig. 10, B**)**, as was reported earlier (27). However, its concentration shows a remarkably higher variability (CV~26%) (Fig. 10, E, Table 4). Essentially, the methanol permeabilization used for DAPI staining (Methods, Section 1.2) did not affect the variability of HU and DnaA (data not shown).

The correlation between the concentrations of DnaA and HU is relatively weak with a covariance value of 0.73 (Fig 10, F). This cloudy relationship may be better characterized by the variation of each of them expressed as:

$$\eta^2_{DnaA} = \frac{\langle (d-h)^2 \rangle}{2\langle d \rangle \langle h \rangle}; \eta^2_{HU} = \frac{\langle dh \rangle - \langle d \rangle \langle h \rangle}{\langle d \rangle \langle h \rangle}$$

where *d* and *h* are cell concentrations of DnaA and HU, respectively, and angled brackets denote the average over the population. The values of this variation, 0.024 for DnaA and 0.050 for HU calculated for the same population support a much lower variability of DnaA concentration than that of HU. These features show the lack of synchrony in the variability of DnaA and HU.

The ratio of DnaA/HU is almost volume-independent (Fig. 11), and its variance is notable (Table 4). Moreover, the variance is age-dependent – higher in smaller cells, decreasing towards division (Fig. 11, orange line, Table 4). Notably, in a slow-growing culture, variabilities of DnaA and HU concentrations but not their ratio variability are lower than in a fast-growing culture and the difference between young and adult cells is less pronounced (Table 4 and Fig. S3). These

variabilities are much lower in cells treated with CAM or RIF (Table S3, Fig. S4). This might be the replication and division runout outcome, producing completed chromosomes segregated into smaller cells independently of the initially varying DNA content (see also the insets to panels B and E in Fig. 2).

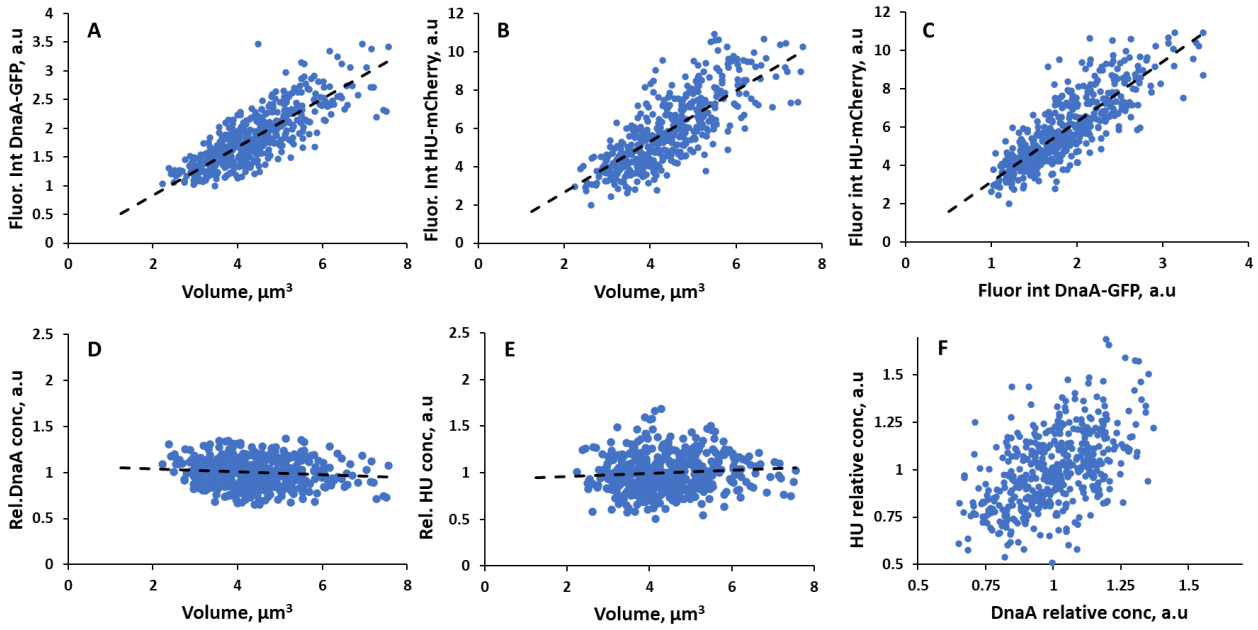

Fig. 10. DnaA and HU amounts and concentrations in cells of different sizes in a population. Approximately 500 cells from a steady-state culture grown in the Neidhardt medium (generation time 32 min) were measured. The image analysis was performed using ImageJ with the ObjectJ plugin and Coli-inspector protocol ((35) and see Methods for details). The dependences of total cellular fluorescence intensities of DnaA-GFP **(A)** and HU-mCherry **(B)** on cell volume and their mutual relation **(C)** are shown. The data were fitted to a linear function (dashed lines, y = 0.42x, R = 0.81 for **A**, y = 1.33x, R = 0.77 for **B**, and y = 3.14x, R=0.82 for **C**). The corresponding dependences of DnaA **(D)** and HU **(E)** concentrations (normalized to the population average) on cell volume are shown. **F** - The relationship between DnaA and HU normalized concentrations.

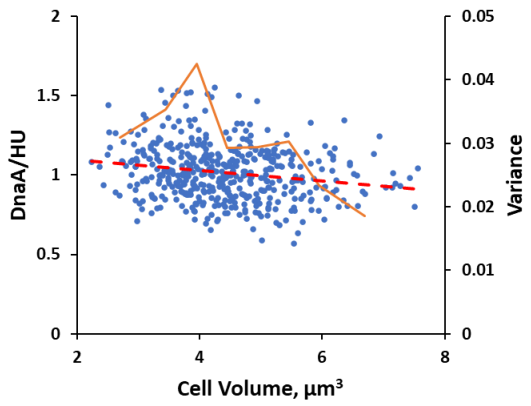

Fig. 11. Dependence of the DnaA/HU ratio normalized per the population average (blue circles and red dashed linear fit) on the cell volume. Orange segmented line – variance of DnaA/HU in different cell size classes after binning of 0.5 µm^3.

Table 4. Variance of DnaA and HU normalized concentrations and their ratio in the cell population as shown in Fig. 10 (D, E) and Fig. 11.

		Fast growing (CV)	Slow growing (CV)
HU		0.067 (0.26)	0.049 (0.22)
DnaA		0.032 (0.18)	0.027 (0.16)
DnaA/HU	population	0.028 (0.17)	0.025 (0.16)
	young†	0.028 (0.17)*	0.026 (0.16)**
	adult†	0.024 (0.15)*	0.025 (0.16)**

†Young – subpopulation of cells smaller than median volume (4.38 µm^3 for fast-growing and 1.56 µm^3 for slow-growing), Adult - larger than median volume; * $p < 0.002$; ** p >- 0.05.

Discussion

In live cells, the protein fluorescence was well associated with the nucleoid body highlighted by HU-mCherry (Fig. 1). Although its distribution was somewhat heterogeneous, we did not observe distinct foci or helixes as reported for similar constructs in *E. coli* and *B. subtilis* (22-24). This may be due to a different imaging setting optimized for collecting multiple sample fields to reveal the population variability (see Methods, Section 1.2).

Both the spot position and the pixel-to-pixel colocalization analyses (Section 1.1 of Results) indicate a significant overlap in the location of HU-mCherry and DnaA-GFP in live

cells, suggesting the tight association of DnaA with the nucleoid. This is supported by the low mobility of DnaA obtained by FRAP (Table 3): although it is one order faster than that of HU, it is one order slower than that of DnaA(L417P) or free GFP. This is consistent with the binding-diffusion mode of its motion reported by single-molecule tracking (24). The wider than HU-mCherry fluorescence intensity profiles of DnaA-GFP (Fig. 1) and the moderate Manders overlap coefficient (Table S1) imply that a part of DnaA resides in the nucleoid periphery or is unbound. The last option could not be examined due to the limited temporal resolution of FRAP at the long acquisition time (see Methods). In fact, DnaA readily dissociates from the released nucleoids in contrast to HU (Section 3 of Results). The attempt to increase the nucleoid-free cytoplasmic volume by arresting protein or DNA synthesis brought an unexpected result (see below).

HU content perfectly correlates with the cell size (Fig. 10B), and with DAPI staining (27); moreover, it follows DAPI distribution within the cell (Fig. 4 and 5A) population-wide, representing the DNA content of nucleoids. This is obviously due to the huge number of HU binding sights over the entire chromosome length (37). Within released nucleoids, the distribution of HU and DAPI looks somewhat different (Fig. 8), presumably reflecting their different DNA topology-dependent binding modes (38). The analysis of the cell asymmetry indexes (Fig. 4 and 5) indicates that DNA material is distributed unevenly within the cell, suggesting asymmetric nucleoid segregation. On average, more DNA is found in the half of a larger volume (Fig. 4A) consistent with the reported in (39). (Note, that the volume is larger essentially due to the larger diameter since the cell length is equally divided in our calculation method). The correlation is weak and has a high variance, meaning that a larger nucleoid is not necessarily partitioned into cell half of a larger volume. DNA concentration thus negatively correlates with the volume (Fig. 4B) and its asymmetry index in HU-aligned cells is about 1.15 (Table 2). The consequence of this intracellular asymmetry is the high intercellular variability of HU concentrations in a population (Fig. 10, E, F; Table 4). We note also the same CVs of asymmetry indexes and the cellular concentrations (Tables 2 and 4).

DnaA does not necessarily follow the distribution of HU or DAPI and appears well equilibrated between the cell halves. The amount of DnaA also correlates with the cell

volume (Fig. 10A), but its concentration asymmetry of cell halves is close to 1, at any cell alignment (Table 2). So how does the intercellular variability of DnaA concentration develop? The different DnaA/DNA ratios in divided cells should be created due to the high asymmetry in DNA concentration in the mother cell. Accordingly, the DnaA/DNA ratio varies in cells (Table 4), with a larger variance in younger cells than in adults (Fig. 11 and Table 4). Comparing the variability of HU (CV=26%), DnaA, and their ratio (both with CV=18%) (Table 4) together with the appreciable correlation between DnaA and HU concentrations (covariance value of 0.73, Fig. 10F), it can be concluded that HU and DnaA are not completely independent variables. Namely, a larger nucleoid can bring more bound DnaA to a newborn cell. The low fraction of free DnaA (total (40) minus bound (15)) may be considered as a low-copy-number noise factor. Thus, DnaA/DNA variability may lead to a variable next replication initiation time – initiation noise. At least partial equilibration of DnaA between multiple nucleoids along filamentous cells may establish higher synchrony of initiations, supporting the explanation of our previous findings (9).

The estimated initiation asynchrony index of 0.14 for fast-growing *E. coli* (41) is compatible with our 1.15 intracellular asymmetry of HU. Analyzing some discrepancies between cell mass and chromosome content of cells treated with CAM or Rif in their pioneer work, Skarstad *et al*. noted that they reflect "the cell-to-cell variation in initiation and termination ages" (42, 43). In addition, fast oscillations of DnaA between cell halves with a period of about 5 sec were detected in *E. coli* (24). Such oscillations may occasionally initiate replication in one of the two nucleoids only. Fast inactivation of DnaA-ATP just after the initiation (16) would delay the initiation in the nucleoid in the other cell half. The nature of these DnaA oscillations is unknown but their possible relation to the "longitudinal density waves'' in replicating nucleoids in the same time scale (44) seems very intriguing. Could it be that DnaA is 'relocated' by these waves along or between nucleoids?

Asynchronous initiation at different oriCs may be, in turn, a plausible origin of the asymmetric DNA distribution within the cell. At our growth conditions, newborn cells contain two already initiated nucleoids (with 4 oriCs) and four nucleoids in cells approaching division (Fig. 2, A). Two pairs of new replication forks in one nucleoid can accumulate 15%

asymmetry in the DNA content of nucleoids during a 3–4-minute difference in initiation times. This period is well comparable with the average time difference (asynchrony) between nucleoid segregation events in cell lineages (9). The intercellular HU concentration varies even more (CV = 26% (Table 4)) suggesting an additional uncertainty factor. The asymmetric cell division (39, 45) is suggested to be such a factor. This type of asymmetry was not explored in this work.

We suggest the variability of DnaA/DNA ratio as the main factor of the variable replication initiation time in *E. coli* (see Scheme 1). This can explain the increasing asynchrony in the nucleoid segregation in a growing cell lineage reported in our previous work (9). Moreover, the high variability in the time of start of septation (CV of ~30%, (46)) may also result from variabilities in replication initiation and nucleoid segregation, permitting the Z-ring formation.

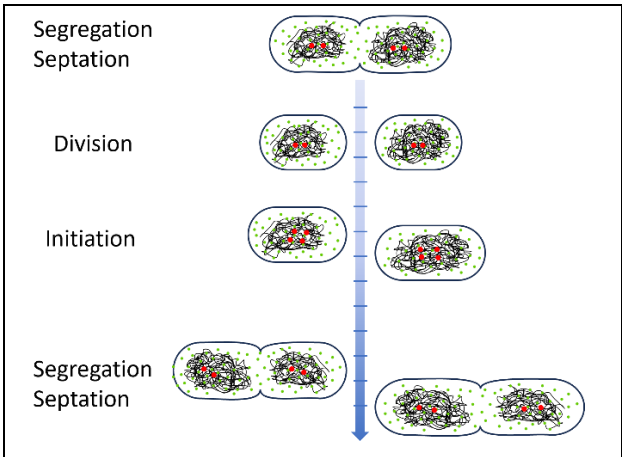

Scheme 1. Generation of cell-to-cell variability by asynchronous initiation. Asymmetric DNA segregation (black line mesh) and homogeneous DnaA distribution (green dots) result in different DnaA/DNA ratios in daughter cells (larger in the left one). This cell will initiate earlier than the right one, leading to an earlier segregation and division. The extended growth time of the right cell will be completed in lengthier daughters. Red dots – oriCs.

In the slow-growing *E. coli* population the variabilities of HU and DnaA are lower (Table 4) apparently because of the lower number of oriCs per cell (one or two) and the initiation and corresponding termination are within the same cycle. The resulting initiation asynchrony index measured in the same strain was 0.06 – distinctly lower than 0.14 in fast-growing cells (41). The fact that DnaA/HU variance is not decreased to the same extent may indicate significant division asymmetry, generating daughter cells with an equal amount of DNA but a higher amount of DnaA in the larger cell.

Attempting to discriminate between nucleoid-associated and freely diffusing DnaA, we exploited cells with different nucleoid/cytoplasm volume ratios: with nucleoid compacted after CAM treatment or expanded cytoplasm in elongated NAL-treated cells (Fig. 1, second and third rows). As a result, DnaA appears to 'spread' outside the nucleoid (see the corresponding fluorescence profiles in Fig. 1). Unexpectedly, the diffusion of DnaA in cytoplasmic areas of both kinds of cells was even slower than in untreated cells (Table 3, Supplementary Fig. S2). This slow diffusion may be attributed to the DnaA bound to the few high-affinity DnaA-boxes on the DNA strands outside the compacted nucleoid body. CAM inhibits ribosome translocation and stabilizes mRNAs (47) while the RNA synthesis persists (21, 48). Super-resolution microscopy reveals 46% of bound RNAP in the periphery of nucleoids compacted by CAM treatment (49). Our visual impression of the compacted nucleoid boundaries may be misleading, while the HU and DAPI fluorescence intensity profiles display, in addition to the central narrow peak, noticeable shoulders covering the rest of the cell (Fig. S5). This profile can be deconvolved into two Gaussian peaks – one high and narrow, corresponding to the bright nucleoid body, and another low but stretched over the cell length (Fig. S5). Given the ten-times difference between the peaks' amplitudes the cell-wide 'background' is hardly identified by the eye, though comprising about 40% of the total cellular fluorescence intensity (comparable with the percent of the bound RNAP). This assumption regarding DNA distribution in CAM or NAL-treated cells and the corresponding DnaA binding requires further investigation beyond the aims of this study.

The major cell cycle event in bacteria – the initiation of chromosome replication, is believed to be controlled by two mechanisms: accumulation of DnaA to the threshold level (14) and regulation of the DnaA activity (ATP/ADP forms) (16), or both (17). The timing of this event and its relation to the cell size (the 'initiation mass') was a matter of interest for many decades (50). Although the data presented here are insufficient to distinguish between free and bound DnaA, nor its ATP/ADP form, it is understandable that the time required to establish the conditions for initiation depends on the starting conditions of the cell, e.g. cell size, DnaA content, growth rate, etc. In one of the more recent works, this question was examined by changing the cell size (51). It was concluded that in *E. coli* the cellular amount of DnaA, rather than its concentration, is decisive for the initiation timing. We now specify

that the DnaA/DNA ratio may be a more rigorous feature in determining the variability of initiation time in *E. coli*.

Materials and Methods

1. Strains and sample preparation

1.1. Strains and plasmids

MG1655 strain of *E. coli* was used in this study carrying chromosomal copies of two genes in their original loci, *dnaA* and *hupA*, fused in frame with fluorescent reporters, *egfp* and *mCherry*, respectively. The construction of the strain is described in Supplemental Material.

DnaA(L417P)-mCherry and eGFP proteins were expressed in the wild-type MG1655 transformed with pBAD24 plasmids carrying the corresponding genes (36) by the addition of 0.2% arabinose for 2.5 hours.

Antibiotic treatment (where relevant) was performed at 37°C with 100 µg/mL CAM, 180 µg/mL Rif for 60 minutes, and 30 µg/mL NAL for 30 minutes. Cells transformed with pBAD24 plasmids containing antibiotic resistance were grown with 50 µg/mL ampicillin. For FRAP experiments, cells were treated with low Cephalexin (15 µg/mL) for one generation time.

1.2. Sample preparation for microscopy, image acquisition and processing

E. coli MG1655 (*dnaA-gfp*, *hu-mcherry*) were grown exponentially for 8-10 generations in Neihardt's medium (52) (basal plus supplement) (FORMEDIUM LTD, Hunstanton, England) at 37°C to optical density 0.2 at 600 nm. Generation time was 32 min in the full medium and 65 min without the supplement. For microscopy, cells from steady-state cultures were loaded on Neihardt's 2% agarose gel pads and imaged at room temperature. For DAPI staining, cells were washed twice with PBS by centrifugation at 16,000xg for 5 minutes at 4°C and the final pellet was resuspended in ice-cold PBS containing 10% methanol. The permeabilized cells were stained with 1.5 µM DAPI and loaded on PBS 2% agarose pads.

Images were taken using a Zeiss Axiovert 200M fluorescence microscope equipped with a 100 ×/1.4 plan-apochromat objective, and an AxioCam HRm camera. The microscope operation and image acquisition were controlled by the AxioVision SE (V4.9.1.0) program. A reduced light intensity (1D neutral filter in the excitation light path) was used to minimize the photobleaching of fluorophores during multifield acquisition. Images of DnaA-GFP and HU-mCherry were acquired with corresponding filter sets and exposure times of 5 sec and 500 msec, respectively. The GFP, mCherry, and DAPI images were subjected to a "rolling ball" background subtraction routine of ImageJ (53) using the 80-pixel ball radius. To decrease the noise level in DnaA-GFP images, an additional background creation with a 1-pixel ball radius was performed. Images of approximately 500 cells were acquired, processed, and analyzed using the Coli-Inspector project of the ObjectJ plugin for ImageJ (35).

1.3. Spheroplasts preparation and release of nucleoids

To estimate the binding affinity of HU and DnaA to the nucleoid, we used to release nucleoids from cells and measure the extent of retained proteins relative to that in intact cells. The bacteria were grown as described above. 3 μM DAPI was added for DNA staining. The lysozyme-induced spheroplasts were prepared as described in (54). Briefly, 10 ml samples of cells from steady-state growing cultures were centrifuged (5 min, 16,000 g, room temperature), and pelleted cells were resuspended in cold 0.8 ml buffer A (0.01M Tris, pH8, 0.1M NaCl, 20% sucrose) and 0.2 ml buffer B (0.12M Tris, pH 7.7, 0.05M EDTA, 0.4 mg/ml lysozyme). In 20–30 min of incubation on ice, ~90% of the cells were converted to spheroplasts.

The nucleoids were released from the spheroplasts heated at 37°C for 10 minutes, loaded on the agarose pads prepared using buffer A, and immobilized on the agarose surface (Fig. 7 and 8 of Results, Section 3).

The fluorescence intensities of DnaA-GFP and HU-mCherry of released nucleoids were calculated using the DAPI-stained images of nucleoids as a mask. The GFP/DAPI and mCherry/DAPI ratios of fluorescence intensities in cells, spheroplasts, and released nucleoids were normalized to the average intensity ratios of intact cells.

2. Intracellular spatial distribution of DnaA-GFP and HU-mCherry

2.1. Scatter Plot of Spot Positions.

The localization of DnaA-GFP and HU-mCherry was analyzed using the Coli-Inspector plugin for ImageJ (35). "Spots", identified as the fluorescence maxima positions for each fluorophore, were generated by setting the tolerance limit at about 80% of the intensity maximum. The spot number for HU-mCherry was verified empirically according to the expected number of nucleoids in the cell, either from the CCSim simulation (55) or experimentally found for the same strain and conditions (9). At our conditions, this number is between 2 and 4 nucleoids per cell, well detected with appropriate tolerance (Fig. 2. A). For generating the spots of DnaA-GFP we followed the approach of Nozaki et al. (22). About 500 cells were analyzed in a population, and the histogram of HU spot numbers (i.e. number of nucleoids) well correlates with the cell size distribution (compare Fig. 2, insets, and Fig. S1). A similar distribution was observed for DnaA spots (Fig. 2, B). Spots' positions for DnaA-GFP and HU-mCherry relative to a cell pole were obtained and plotted to examine colocalization. DnaA and HU spots were also paired based on the closest proximity and the corresponding distances between them were calculated.

2.2. Cytofluorogram: pixel intensity-based correlation

In pixel-wise colocalization analyses, the intensity of a pixel in one channel is evaluated against the corresponding pixel in the second channel of a dual-color image, producing a scatterplot from which a correlation coefficient is determined. The ImageJ plugin JaCoP (25) (https://imagej.net/plugins/jacop) was used to generate scatterplots and to characterize the degree of colocalization (26). The cytofluorograms normalized to the intensities' maxima were converted to color-coded density scatter plots using MATLAB routine.

3. Population analysis and cell asymmetry measurement

The cellular amounts and concentrations of DnaA and HU were analyzed in a cell population by exploiting the single genome copies of *dnaA-gfp* and *hu-mcherry* (see Section 1.1)., The total fluorescence intensity per cell served as a measure of the tagged protein amount in the cell since every DnaA and HU protein carries its fluorescent tag. Integral cell fluorescence in both GFP and

mCherry channels, as well as the dimensions of corresponding cells, were obtained using the "Coli Inspector" program as described in (35). Concentrations of DnaA and HU were calculated by dividing the total cell fluorescence intensity by the cell volume.

Cell diameter and fluorescence intensity profiles along each cell in a population are collected and stored in a "Map" image (Fig. 12, A). In these maps, each cell is shown as a line of the corresponding length in pixels, where the brightness of each pixel along the line corresponds numerically to the cell diameter (d, in pixel) or fluorescence intensity integral of a cell cross-section (slice) at this point. As each pixel-wide slice of a (rod-shaped) cell is close to a disk shape, its volume V_c can be calculated as $V_c = \pi(d/2)^2$ cubic pixels. The whole cell volume (or its part) can be thus calculated more accurately as a sum of corresponding slices instead of using mean cell diameter. Amounts and concentrations of DnaA-GFP, HU-mCherry, and DAPI are also calculated more reliably using the volume calculated in this way.

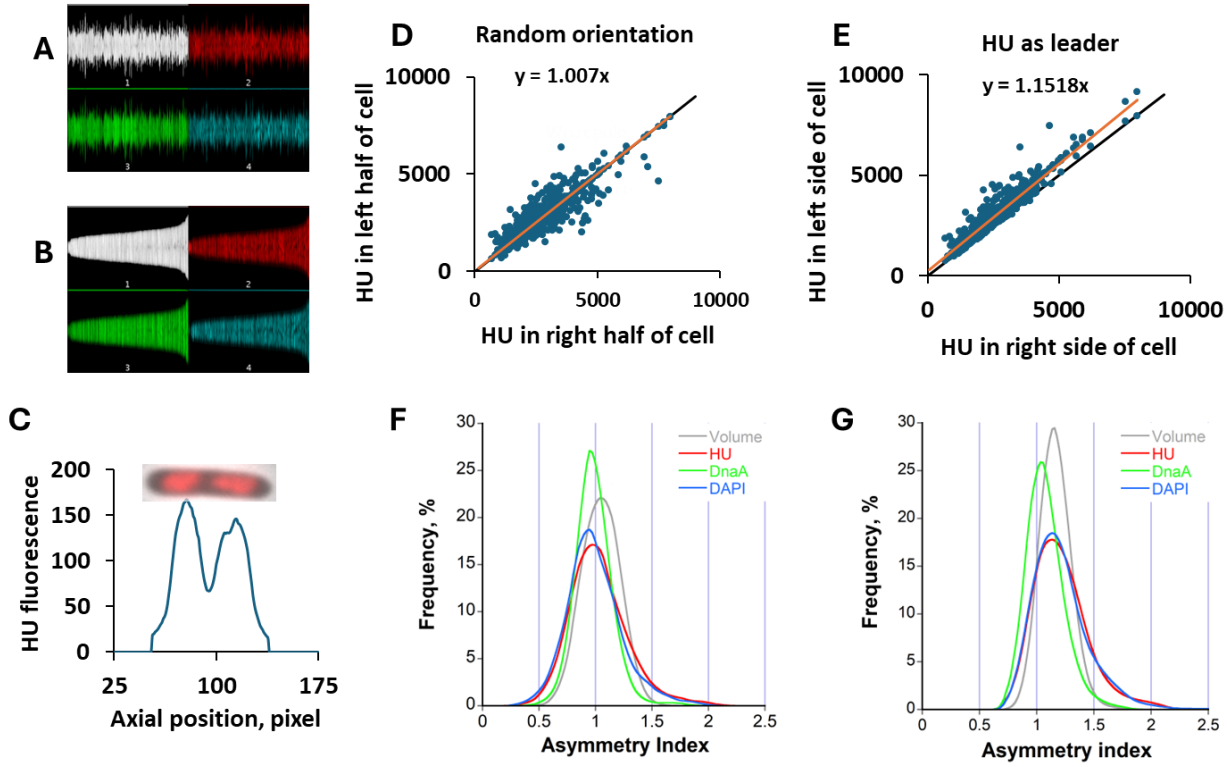

Fig. 12. A. Profiles maps of diameter (white), and fluorescence intensities of HU-mCherry (red), DnaA-GFP (green), and DAPI (blue) in a population. **B.** 'Sorted' map: same profiles as in **A** but sorted according to cell length. **C.** Profile of the HU-mCherry fluorescence along an individual cell

(above) with apparently more HU in the left half (the leader pole). **D-E.** Relation between HU integral fluorescence in cell halves in randomly oriented **(D)** or aligned **(E,** HU as the leader pole**)** populations; equality line (black) and the linear fit (orange) are shown. **F-G.** Histograms of asymmetry indexes for volume (grey), HU (red), DnaA (green), and DAPI (blue) in random population (**F**) and aligned for each property (**G**).

The map can be sorted according to the cell length or other measured parameters (Fig. 12, B). Furthermore, the cells in a map can be aligned ('flipped' map) according to the wider or higher intensity cell half ('leader pole'). In this case, all cells in the map are oriented with the leader pole in the same direction allowing analysis of intracellular distributions of different (labeled) components. This way, the ratios of volumes, and integral fluorescence intensities between the cell halves (half length) were calculated for random populations or aligned using different leader poles. In a randomly oriented population, the ratios of all quantities in cell halves (asymmetry indexes) are distributed around 1 (Fig. 12, D, F). It was obtained occasionally slightly larger or smaller than 1 experimentally (Fig. 5, Table 2, no leader pole), reflecting the one-pixel accuracy of the mid-cell demarcation. After alignment, the asymmetry indexes become larger than 1 (Fig. 12, E, G), revealing a single-cell asymmetry distribution (exemplified in Fig. 12, C) in the whole population.

The asymmetry index was thus calculated using the ratio of amounts or concentrations of HU, DnaA, and DNA in the two halves of each cell and averaged over the population. Alternatively, this index can be derived from the slope of linear regression fit to the corresponding values in cell halves for the whole population (Fig. 12, D, and E).

4. Protein mobility measurement using FRAP

Zeiss Axio-Observer 7 inverted microscope (Zeiss) was used with 3i Marianas (Denver, CO) spinning disk confocal microscope equipped with Yokogawa W1 module (Yokogawa) and Prime 95B sCMOS camera (pixel size 0.106 microns) (Photometrics). The acquisition was controlled using SlideBook software (Intelligent Imaging Innovations, SlideBook v2304).

The pre-bleaching and recovery frames were acquired at 100% illumination for both channels. The ROI area of 0.90 μm^2 was exposed to 100% power of 488 nm laser photobleaching GFP and mCherry. Two frame intervals were used – 2 sec and 500 msec for 3 minutes and 50 seconds recovery kinetics of HU-mCherry and DnaA-GFP, respectively.

Fluorescence intensities of the chosen ROIs were measured after background subtraction using the 80-pixel rolling ball routine. The acquisitional bleaching of control (unbleached) cells was used for the data correction and normalization. The recovery half-time of DnaA and HU for each cell was derived from the single exponential fit generated by KaleidaGraph software (Synergy software, version 4.0). The predicted maximal recovery was calculated from the total cell and the bleached ROI areas. The diffusion coefficients of DnaA and HU were obtained using the simFRAP plugin version 0.95 (28) for Fiji software (56) based on simulating a 2-D random walk in each pixel of bleached ROI.

Acknowledgments

This research was partially supported by the Israel Science Foundation (Grant# 1519/18 for IF and MF). The Scholarship to SKN was provided by the Kreitman School for Advanced Studies, Ben Gurion University of Negev. Dr. Maria Vyazmensky is appreciated for the technical assistance.

References

1. Avery SV. 2006. Microbial cell individuality and the underlying sources of heterogeneity. Nat Rev Microbiol 4:577-87.
2. Lidstrom ME, Konopka MC. 2010. The role of physiological heterogeneity in microbial population behavior. Nat Chem Biol 6:705-12.
3. Reuven P, Eldar A. 2011. Macromotives and microbehaviors: the social dimension of bacterial phenotypic variability. Curr Opin Genet Dev 21:759-67.
4. Balaban NQ. 2011. Persistence: mechanisms for triggering and enhancing phenotypic variability. Curr Opin Genet Dev 21:768-75.
5. Elowitz MB, Levine AJ, Siggia ED, Swain PS. 2002. Stochastic gene expression in a single cell. Science 297:1183-6.
6. Huh D, Paulsson J. 2011. Non-genetic heterogeneity from stochastic partitioning at cell division. Nat Genet 43:95-100.
7. Rosenfeld N, Young JW, Alon U, Swain PS, Elowitz MB. 2005. Gene regulation at the single-cell level. Science 307:1962-5.

8. Norris V, den Blaauwen T, Doi RH, Harshey RM, Janniere L, Jimenez-Sanchez A, Jin DJ, Levin PA, Mileykovskaya E, Minsky A, Misevic G, Ripoll C, Saier M, Jr., Skarstad K, Thellier M. 2007. Toward a hyperstructure taxonomy. Annu Rev Microbiol 61:309-29.
9. Gelber I, Aranovich A, Feingold M, Fishov I. 2021. Stochastic nucleoid segregation dynamics as a source of the phenotypic variability in E. coli. Biophys J 120:5107-5123.
10. Cass JA, Kuwada NJ, Traxler B, Wiggins PA. 2016. Escherichia coli Chromosomal Loci Segregate from Midcell with Universal Dynamics. Biophys J 110:2597-2609.
11. Nielsen HJ, Li Y, Youngren B, Hansen FG, Austin S. 2006. Progressive segregation of the Escherichia coli chromosome. Mol Microbiol 61:383-93.
12. Nielsen HJ, Youngren B, Hansen FG, Austin S. 2007. Dynamics of Escherichia coli chromosome segregation during multifork replication. J Bacteriol 189:8660-6.
13. Woldringh CL, Hansen FG, Vischer NO, Atlung T. 2015. Segregation of chromosome arms in growing and non-growing Escherichia coli cells. Front Microbiol 6:448.
14. Hansen FG, Atlung T. 2018. The DnaA Tale. Front Microbiol 9:319.
15. Roth A, Messer W. 1998. High-affinity binding sites for the initiator protein DnaA on the chromosome of Escherichia coli. Mol Microbiol 28:395-401.
16. Katayama T, Kasho K, Kawakami H. 2017. The DnaA Cycle in Escherichia coli: Activation, Function and Inactivation of the Initiator Protein. Front Microbiol 8:2496.
17. Berger M, Wolde PRT. 2022. Robust replication initiation from coupled homeostatic mechanisms. Nat Commun 13:6556.
18. van Helvoort JM, Kool J, Woldringh CL. 1996. Chloramphenicol causes fusion of separated nucleoids in Escherichia coli K-12 cells and filaments. J Bacteriol 178:4289-93.
19. Deitz WH, Cook TM, Goss WA. 1966. Mechanism of action of nalidixic acid on Escherichia coli. 3. Conditions required for lethality. J Bacteriol 91:768-73.
20. Bakshi S, Choi H, Mondal J, Weisshaar JC. 2014. Time-dependent effects of transcription- and translation-halting drugs on the spatial distributions of the Escherichia coli chromosome and ribosomes. Mol Microbiol 94:871-87.
21. Cabrera JE, Cagliero C, Quan S, Squires CL, Jin DJ. 2009. Active transcription of rRNA operons condenses the nucleoid in Escherichia coli: examining the effect of transcription on nucleoid structure in the absence of transertion. J Bacteriol 191:4180-5.
22. Nozaki S, Niki H, Ogawa T. 2009. Replication initiator DnaA of Escherichia coli changes its assembly form on the replication origin during the cell cycle. J Bacteriol 191:4807-14.
23. Boeneman K, Fossum S, Yang Y, Fingland N, Skarstad K, Crooke E. 2009. Escherichia coli DnaA forms helical structures along the longitudinal cell axis distinct from MreB filaments. Mol Microbiol 72:645-57.
24. Schenk K, Hervas AB, Rosch TC, Eisemann M, Schmitt BA, Dahlke S, Kleine-Borgmann L, Murray SM, Graumann PL. 2017. Rapid turnover of DnaA at replication origin regions contributes to initiation control of DNA replication. PLoS Genet 13:e1006561.
25. Bolte S, Cordelieres FP. 2006. A guided tour into subcellular colocalization analysis in light microscopy. J Microsc 224:213-32.
26. Dunn KW, Kamocka MM, McDonald JH. 2011. A practical guide to evaluating colocalization in biological microscopy. Am J Physiol Cell Physiol 300:C723-42.

27. Abebe AH, Aranovich A, Fishov I. 2017. HU content and dynamics in Escherichia coli during the cell cycle and at different growth rates. FEMS Microbiol Lett 364.
28. Blumenthal D, Goldstien L, Edidin M, Gheber LA. 2015. Universal Approach to FRAP Analysis of Arbitrary Bleaching Patterns. Sci Rep 5:11655.
29. Stracy M, Schweizer J, Sherratt DJ, Kapanidis AN, Uphoff S, Lesterlin C. 2021. Transient non-specific DNA binding dominates the target search of bacterial DNA-binding proteins. Mol Cell 81:1499-1514 e6.
30. Bettridge K, Verma S, Weng X, Adhya S, Xiao J. 2021. Single-molecule tracking reveals that the nucleoid-associated protein HU plays a dual role in maintaining proper nucleoid volume through differential interactions with chromosomal DNA. Mol Microbiol 115:12-27.
31. Bellotto N, Agudo-Canalejo J, Colin R, Golestanian R, Malengo G, Sourjik V. 2022. Dependence of diffusion in Escherichia coli cytoplasm on protein size, environmental conditions, and cell growth. Elife 11.
32. Breusegem SY, Clegg RM, Loontiens FG. 2002. Base-sequence specificity of Hoechst 33258 and DAPI binding to five (A/T)4 DNA sites with kinetic evidence for more than one high-affinity Hoechst 33258-AATT complex. J Mol Biol 315:1049-61.
33. Schaper S, Messer W. 1995. Interaction of the initiator protein DnaA of Escherichia coli with its DNA target. J Biol Chem 270:17622-6.
34. Pelletier J, Halvorsen K, Ha BY, Paparcone R, Sandler SJ, Woldringh CL, Wong WP, Jun S. 2012. Physical manipulation of the Escherichia coli chromosome reveals its soft nature. Proc Natl Acad Sci U S A 109:E2649-56.
35. Vischer NO, Verheul J, Postma M, van den Berg van Saparoea B, Galli E, Natale P, Gerdes K, Luirink J, Vollmer W, Vicente M, den Blaauwen T. 2015. Cell age dependent concentration of Escherichia coli divisome proteins analyzed with ImageJ and ObjectJ. Front Microbiol 6:586.
36. Regev T, Myers N, Zarivach R, Fishov I. 2012. Association of the chromosome replication initiator DnaA with the Escherichia coli inner membrane in vivo: quantity and mode of binding. PLoS One 7:e36441.
37. Ali Azam T, Iwata A, Nishimura A, Ueda S, Ishihama A. 1999. Growth phase-dependent variation in protein composition of the Escherichia coli nucleoid. J Bacteriol 181:6361-70.
38. Huang L, Zhang ZF, McMacken R. 2021. Interaction of the HU Protein with Various Topological Forms of DNA. Biomolecules 11:1724.
39. Huls PG, Vischer NOE, Woldringh CL. 2018. Different Amounts of DNA in Newborn Cells of Escherichia coli Preclude a Role for the Chromosome in Size Control According to the "Adder" Model. Front Microbiol 9:664.
40. Hansen FG, Atlung T, Braun RE, Wright A, Hughes P, Kohiyama M. 1991. Initiator (DnaA) protein concentration as a function of growth rate in Escherichia coli and Salmonella typhimurium. J Bacteriol 173:5194-9.
41. Olsson JA, Nordstrom K, Hjort K, Dasgupta S. 2003. Eclipse-synchrony relationship in Escherichia coli strains with mutations affecting sequestration, initiation of replication and superhelicity of the bacterial chromosome. J Mol Biol 334:919-31.
42. Lobner-Olesen A, Skarstad K, Hansen FG, von Meyenburg K, Boye E. 1989. The DnaA protein determines the initiation mass of Escherichia coli K-12. Cell 57:881-9.

43. Skarstad K, Boye E, Steen HB. 1986. Timing of initiation of chromosome replication in individual Escherichia coli cells. EMBO J 5:1711-7.
44. Fisher JK, Bourniquel A, Witz G, Weiner B, Prentiss M, Kleckner N. 2013. Four-dimensional imaging of E. coli nucleoid organization and dynamics in living cells. Cell 153:882-95.
45. Biswas K, Sanderson AE, Salman H, Brenner N. 2024. Single-cell Growth Rate Variability in Balanced Exponential Growth. bioRxiv doi:10.1101/2024.06.23.600237:2024.06.23.600237.
46. Reshes G, Vanounou S, Fishov I, Feingold M. 2008. Timing the start of division in E. coli: a single-cell study. Phys Biol 5:046001.
47. Lopez PJ, Marchand I, Yarchuk O, Dreyfus M. 1998. Translation inhibitors stabilize Escherichia coli mRNAs independently of ribosome protection. Proc Natl Acad Sci U S A 95:6067-72.
48. Kurland CG, Maaloe O. 1962. Regulation of ribosomal and transfer RNA synthesis. J Mol Biol 4:193-210.
49. Stracy M, Lesterlin C, Garza de Leon F, Uphoff S, Zawadzki P, Kapanidis AN. 2015. Live-cell superresolution microscopy reveals the organization of RNA polymerase in the bacterial nucleoid. Proc Natl Acad Sci U S A 112:E4390-9.
50. Herrick J, Kohiyama M, Atlung T, Hansen FG. 1996. The initiation mess? Mol Microbiol 19:659-66.
51. Hill NS, Kadoya R, Chattoraj DK, Levin PA. 2012. Cell size and the initiation of DNA replication in bacteria. PLoS Genet 8:e1002549.
52. Neidhardt FC, Bloch PL, Smith DF. 1974. Culture medium for enterobacteria. J Bacteriol 119:736-47.
53. Schneider CA, Rasband WS, Eliceiri KW. 2012. NIH Image to ImageJ: 25 years of image analysis. Nat Methods 9:671-5.
54. Romantsov T, Fishov I, Krichevsky O. 2007. Internal structure and dynamics of isolated Escherichia coli nucleoids assessed by fluorescence correlation spectroscopy. Biophys J 92:2875-84.
55. Zaritsky A, Wang P, Vischer NOE. 2011. Instructive simulation of the bacterial cell division cycle. Microbiology (Reading) 157:1876-1885.
56. Schindelin J, Arganda-Carreras I, Frise E, Kaynig V, Longair M, Pietzsch T, Preibisch S, Rueden C, Saalfeld S, Schmid B, Tinevez JY, White DJ, Hartenstein V, Eliceiri K, Tomancak P, Cardona A. 2012. Fiji: an open-source platform for biological-image analysis. Nat Methods 9:676-82.